Energy and angular distributions of neutrons from 90 MeV proton and 140 MeV alpha-particle bombardment of nuclei

A. M. Kalend,* B. D. Anderson, A. R. Baldwin, R. Madey, and J. W. Watson
Department of Physics, Kent State University, Kent, Ohio 44242

C. C. Chang, H. D. Holmgren, R. W. Koontz,† and J. R. Wu‡
Cyclotron Laboratory, University of Maryland, College Park, Maryland 20742

H. Machner
Fachbereich Physik, Universität Bremen, D-2800 Bremen 33, Federal Republic of Germany and Institut für Kernphysik der KFA Jülich, D-5170 Jülich, Federal Republic of Germany

(Received 14 January 1983)

We measured neutron time-of-flight spectra from 90 MeV protons and 140 MeV alpha particles bombarding thin targets of Al, Ni, Zr, and Bi at laboratory angles between 20° and 135°. The low-energy (5 to 45 MeV) portions of the spectra were measured with 5 cm diameter by 5 cm deep NE-213 counters at 1 m flight paths with n-γ pulse-shape discrimination. The high-energy (35 to 150 MeV) portions of the spectra were measured with 12.7 cm diameter by 10.2 cm deep NE-102 counters at flight paths of 2.0 to 5.0 m. The proton-induced measured neutron spectra reveal three distinct energy regions: a low-energy evaporation region, a high-energy region dominated by the quasifree scattering process, and an intermediate-energy region dominated by multistep, preequilibrium processes. In the latter two regions, the spectra show strong angular dependence. The alpha-particle induced neutron spectra show these same distinct energy regions plus an exponential falloff above the beam energy per nucleon. The neutron spectra are compared with earlier proton spectra produced also by 90 MeV protons and 140 MeV alpha particles. It is observed that the high-energy portions of the forward-angle neutron and proton cross sections are in ratios consistent with the idea that single nucleon-nucleon scattering dominates. For the heavy-mass targets, the low-energy evaporation regions show neutron yields larger than proton yields. The proton-to-neutron ratios observed in the high-energy continua are interpreted with a quasifree calculation fitted simultaneously to the proton and the neutron spectra. Preequilibrium calculations with the exciton model and the hybrid model reproduce the shape of the experimental angle-integrated energy spectra down to lower energies than the quasifree calculations. The exciton model calculations underestimate the magnitudes of the cross sections, while the hybrid model provides better absolute agreement. One of the preequilibrium calculations uses the method of Mantzouranis and Weidenmüller to predict angular distributions; we find that the predicted angular distributions overestimate the neutron yields at forward angles. The intranuclear-cascade model predicts proton-to-neutron ratios much smaller than experimentally observed in the high-energy forward-angle continua.

NUCLEAR REACTIONS ^{27}Al, ^{58}Ni, ^{90}Zr, ^{209}Bi(p,n), (α,n), E_p=90 MeV; E_α=140 MeV; θ_L=20°–135°; measured $d^2\sigma/d\Omega\, dE$; compared with available experimental proton spectra and with theoretical calculations including PWIA quasifree scattering, preequilibrium exciton, geometry-dependent hybrid, and intranuclear-cascade models.

I. INTRODUCTION

Studies of the nuclear continuum excited in nuclear reactions at medium energies are important for several reasons. First, the excitation of the continuum generally dominates the reaction cross section. Usually over one-half of the total reaction strength is into the nuclear continuum. Clearly, in order to have a good understanding of medium-energy nuclear reactions, we must have a good understanding of how the continuum is excited. Recent studies of the continuum indicate that some parts (viz., the high-energy forward-angle regions) are dominated by single-step processes, while other parts are dominated by multistep processes. It is important to understand better the relative roles of these different processes in order to improve the description of medium-energy nuclear reactions. Finally, it is important also to obtain reliable theoretical understanding of the nuclear continuum in order to subtract properly the continuum as a background from various broad "giant" resonances excited in medium-energy nuclear reactions. There has been much interest in the excitation of such resonances for many years, and the proper subtraction of the continuum remains as one of the large sources of uncertainty in the strength extracted for these states.

There has been a concerted effort, both theoretical and experimental, to develop and test various nuclear models explaining the transitions to the continuum following the interactions of energetic projectiles with nuclei. These theoretical models include simple quasifree scattering cal-

culations, preequilibrium decay models, and intranuclear cascade models. For the testing and critical development of these models, several comprehensive experimental programs[1–6] were undertaken to measure complete spectra of various charged particles emitted from bombardment with medium-energy light-ion projectiles. Similar measurements of neutron continuum spectra are few, especially at bombarding energies above 60 MeV.[5,7–9] Several features of interest have emerged from the studies of charged-particle continuum spectra. In light-ion scatterings at energies above 50 MeV, the dominant reaction channels excite mainly the continuum rather than discrete nuclear states.[2,3,5,6,10] In their studies of emitted charged particles (p,d,t,α) from 90 MeV protons on thin targets (Al, Ni, Zr, and Bi), Wu *et al.*[2] observed that the total yield of the charged particles was about twice the reaction cross section, and that a large fraction of this yield was observed at energies well above the evaporation region. In the high-energy parts of the continuum, broad peaks, or shoulders, were observed in 160 MeV (p,p′) inclusive spectra[1] and found to move down in energy with increasing angle consistent with quasifree nucleon-nucleon scatterings. Wu showed[11] that much of the proton high-energy continuum can be accounted for with a simple quasifree calculation; furthermore, using a combination of the exciton model and the Serber model,[12] Wu and Chang[3] obtained excellent fits to the angle-integrated proton spectra from deuteron bombardment of nuclei. In the spectra of light-charged particles (p,d,t, ^{3}He) from alpha-particle bombardment of nuclei, Wu and Chang also observed so-called "Serber breakup," namely, broad peaks at particle kinetic energies about one-fourth the bombarding alpha-particle energy in the proton spectra, one-half in the deuteron spectra, and three-fourths the bombarding energy in the triton and ^{3}He spectra.

We performed measurements of inclusive neutron spectra at the same proton and alpha-particle bombarding energies as did Wu *et al.*[2,4] The neutron measurements provide important comparisons with the proton measurements. Anderson *et al.*[13] showed that the ratio of emitted neutrons to protons in the high-energy regions of the forward angle spectra are consistent with simple counting arguments and the dominance of the quasifree scattering mechanism. The low-energy portions of the emitted neutron spectra are expected to reveal larger yields than the emitted proton spectra since there exists no Coulomb barrier in the exit channel for neutrons. The simultaneous fitting of both emitted neutron and proton spectra will provide stringent tests for the various models. We present here detailed comparisons of the neutron spectra with the proton spectra of Wu *et al.*[2] and with the predictions of a simple quasifree scattering calculation, an intranuclear-cascade calculation, and preequilibrium-type calculations.

II. EXPERIMENTAL PROCEDURE

A. Experimental arrangement

Neutron energy spectra from 90-MeV protons and 140-MeV alpha particles incident on thin targets of ^{27}Al, ^{58}Ni, ^{90}Zr, ^{197}Au, and ^{209}Bi were measured at the Maryland Isochronous Cyclotron Facility at laboratory angles of 20°, 30°, and up to 135° in steps of 15°. The experimental arrangement is shown in Fig. 1. The incident beam was focused on the target (T) by a quadrupole magnet (QM1) located 3 m upstream of the scattering chamber (SC) and refocused by a quadrupole magnet (QM2) about 5 m downstream of the target into a Faraday cup (FC) within a beam dump outside of the room. Steel, lead, and concrete shielding materials were placed near the downstream quadrupole magnet, as shown in Fig. 1, to reduce background from nuclear interactions of elastically scattered protons from the target.

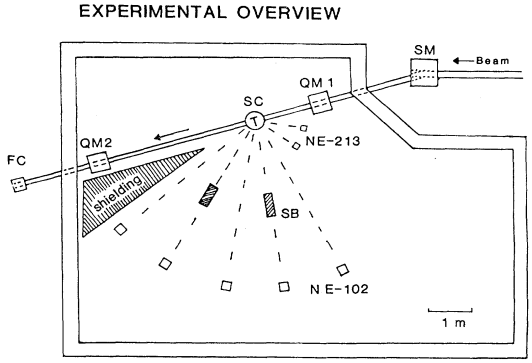

FIG. 1. Floor plan of the experimental arrangement showing a typical placement of neutron counters, shadow shields, and background shielding. SM = switching magnet; QM = quadrupole magnet; SC = scattering chamber; FC = Faraday cup; SB = shadow bar.

Neutron kinetic energies were measured by the time-of-flight (TOF) technique. The high-energy ($\gtrsim$30 MeV) portions of the spectra were measured with 12.7 cm diameter by 10.2 cm deep NE-102 plastic scintillators; the low energy ($\lesssim$30 MeV) portions of the spectra were measured with 5.08 cm diameter by 5.08 cm deep NE-213 liquid scintillators. The flight paths to the front faces of the NE-102 counters were 5.0 m at 20°, 30°, and 45°; 4.0 m at 60°; 3.5 m at 75° and 90°; 3.0 m at 105°; 2.5 m at 120°; and 2.0 m at 135°. The NE-213 counters were always placed at 1 m flight paths. The NE-102 and NE-213 scintillators were coupled to 12.7 cm diameter Amperex XP2041 and 5.08 cm diameter RCA 8575 photomultiplier tubes, respectively. Thin 0.6 cm or 0.3 cm thick NE-102 plastic scintillator counters were placed in front of each neutron detector to veto charged particles. The neutron counters were placed at the same 1.5 m height above the floor as the beam pipe.

Room-scattered backgrounds were measured by performing experimental runs with 12.7 cm diameter by 61 cm long iron shadow shields placed halfway between the target and each detector. The shadow shields attenuated the neutron flux from the target by a factor of at least 100 for all the neutron energies observed in these measurements. The shadow shields were typically placed in front of every other neutron detector, in alternate arrangements.

B. Electronics

The data-acquisition system included a PDP-11/TP-5000 computer with four 12-bit analog-to-digital converters (ADC), commercially available electronics, and specialized electronics developed at Kent State University to

provide increased count-rate and dynamic-range capabilities for fast-neutron spectral measurements. Figure 2 shows a block diagram to illustrate the major components of the electronics.

The anode signal from each counter was split into two signals with a linear fan-out module (LFM). One signal went to a constant-fraction timing discriminator (CFD) which provided a start signal to a time-to-amplitude converter (TAC). The TAC received a stop signal derived from a point of fixed phase on the cyclotron radiofrequency (RF) signal. The output of the TAC went to one of the ADC's to obtain a neutron TOF spectrum. The other anode signal from each LFM went to a linear summing module (LSM) and then to a linear gate and stretcher (LGS) which provided integrated pulse-height (PH) measurements over a 50:1 dynamic range. The output of the stretcher went to a second ADC. Only one TAC and one linear stretcher module were used for all the neutron detectors; signals from different counters were fed into the TAC via an OR/NOR (O/N) module and were identified by a tag word provided to a third ADC by a router (RTR) module.

The anode signal from an NE-213 counter was fanned out twice in order to provide a signal to a pulse-shape discrimination (PSD) module. The PSD module provided a stop signal to a second TAC as shown in Fig. 2. The start signal for this TAC was obtained via a logic fan-out (LFO) module from the CFD of an individual NE-213 counter. The output of this TAC went to the fourth ADC to provide a pulse-shape spectrum for n-γ discrimination.

The ADC's were interfaced to the TP-5000/PDP-11 computer system which listed the data, event by event, on magnetic tape for later off-line analysis, and provided histograms for on-line inspection and analysis.

III. DATA ANALYSIS

The event-by-event list of data recorded on magnetic tape was analyzed off line. Since pulse-height information was recorded for each TOF event, the data could be reanalyzed at any desired threshold above the hardware threshold set by the CFD for each counter. After choosing thresholds, TOF spectra were produced and backgrounds were subtracted using the shadow-shield measurements as described below. For the low-energy portions of the spectra, measured with the NE-213 liquid scintillator detectors, pulse-shape discrimination eliminated gamma-ray events at the level of 0.1% as will be discussed later. The resulting TOF spectra were converted to energy spectra to obtain the yields reported here.

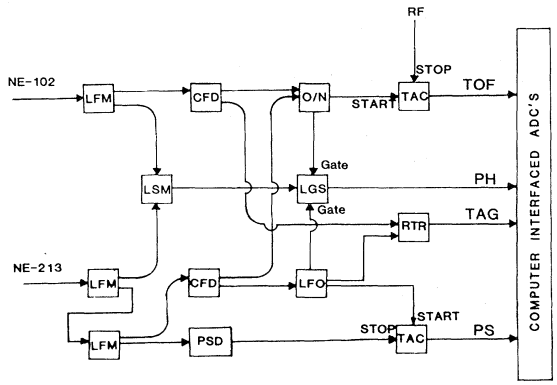

FIG. 2. Block diagram to illustrate the major components of the data acquisition electronics. (See text for defintions of abbreviations.)

A. Background subtraction

Backgrounds, estimated to be primarily from room-scattered neutrons and cosmic rays, were measured by performing a shadow-shield run for each neutron TOF spectrum. The TOF spectra from an aluminum target is shown in Fig. 3(a); the corresponding shadow-shield spectrum is shown in Fig. 3(b). The background spectrum reveals structure in the region from about 4 to 10 MeV neutron energy. We attribute the structure in the measured background to neutrons emitted primarily from the downstream beam line and quadrupole magnet. These neutrons were produced by beam particles elastically scattered in the target which scattered out of the beam line and were stopped in the magnet material near the beam line. The background structure was more pronounced with increasing Z of the target and decreased at more backward angles. In preliminary runs without the shielding in place, we observed very large backgrounds in the most-forward angle counter; subsequently, approximately four feet of steel, lead, and concrete shielding was installed along the beam line, which reduced the forward-angle backgrounds by more than an order of magnitude.

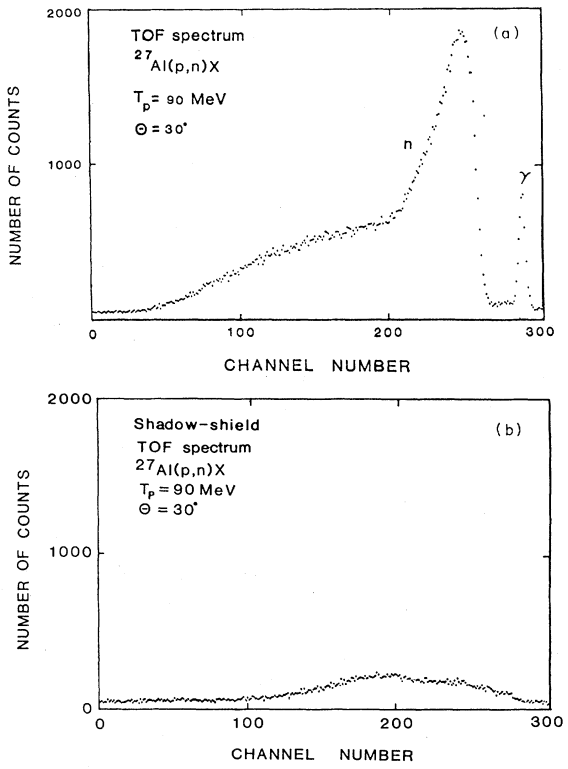

FIG. 3. (a) Typical ^{27}Al(p,n)X time-of-flight spectrum, and (b) its corresponding shadow-shield spectrum. The spectra are from an NE-213 neutron counter at 1 m flight path and at 30°. The pulse-height threshold is 0.6 MeV ee.

Normalized shadow-shield spectra were subtracted channel by channel from the corresponding TOF spectra. The resulting TOF spectra sometimes had small flat residual backgrounds observed at long flight times corresponding to neutron energies below the pulse-height threshold, and at short flight times earlier than the prompt γ peak. The two regions were always at the same height and were only significant for the backward angle spectra where the neutron yields were smallest. We attributed this background to the fact that the shadow shields subtended solid angles which cut off too much of the neutron flux from the target and thereby reduced room-scattered backgrounds. Subsequently a small ($<2\%$) flat background was subtracted (when required) from the TOF spectra.

B. Pulse-height thresholds

Periodically, during the experimental run, each counter was pulse-height calibrated with a series of radioactive gamma sources (viz., ^{22}Na, ^{60}Co, and ^{228}Th). The Compton peak in the gamma-ray spectrum was taken as the calibration point and associated with an energy of an equivalent-electron (ee) equal to 0.95 of the maximum Compton energy.[14] The peaks from the three gamma sources provided pulse-height calibration points for the NE-213 neutron counters. To calibrate the NE-102 neutron counters for large pulse heights, we used a fast linear amplifier (with a measured gain of 10.0) and precision attenuators to amplify the anode signal produced in each NE-102 neutron detector by a ^{228}Th gamma-ray source ($E_\gamma=2.62$ MeV).

Time-of-flight spectra to be analyzed were constructed at pulse-height thresholds of 0.4, 0.5, 0.6, 0.8, 1.0, 1.5, and 2.0 MeV ee for the NE-213 counters and at thresholds of 8.0, 9.0, 10, 11, 12, 14, and 15 MeV ee for the NE-102 neutron counters. A background subtraction was then performed by subtracting from each TOF spectrum its corresponding shadow-shield run at the respective threshold. Pulse-height thresholds for the final analyses were set at 12.0 MeV ee ($\simeq$19 MeV proton energy) for NE-102 neutron counters, and 0.6 MeV ee ($\simeq$2 MeV proton energy) for the NE-213 neutron counters. These thresholds provided the lowest-energy neutron spectra which were consistent with the neutron yields obtained with the higher-threshold analyses.

C. Neutron-gamma discrimination

In the low-energy range ($\lesssim$10 MeV), events from room-scattered gamma-rays and from cosmic rays were comparable in magnitude to real neutron events. These background events were eliminated from the NE-213 TOF spectra by pulse-shape discrimination. For the NE-213 counters, the anode signals were split twice in order to provide inputs to a pulse-shape discrimination (PSD) module based on the circuit of Sperr *et al.*[15] The output of the PSD module went to a TAC module to provide a pulse-shape spectrum as described in Sec. III B.

The pulse-shape spectrum for an aluminum target at 90° is shown in Fig. 4. The pulse-height threshold was set at 0.5 MeV ee. The separation of the neutron and gamma-ray peaks was excellent, providing a figure of merit typically of about 1.2. (The figure of merit is defined as the ratio of the peak separation to the sum of the full widths at half maximum of the gamma-ray and neutron peaks.) For Gaussian peaks, this figure of merit would correspond to a gamma-ray rejection ratio of better than 1000:1.[16] We estimated neutron losses from n-γ discriminations to be typically about 0.2% and at most 1.0% for all the measurements reported here.

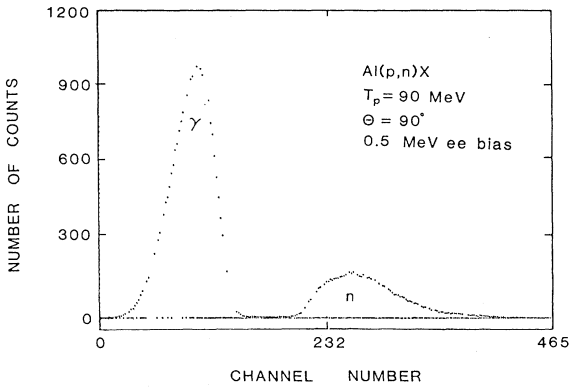

FIG. 4. The pulse-shape spectrum from an aluminum target at a reaction angle of 90°. The pulse-height threshold was set at 0.5 MeV ee.

D. Energy resolutions

For measurements of neutron energies by the TOF method, the fractional energy resolution $\Delta T/T$ is given by the expression

$$\frac{\Delta T}{T}=\gamma(\gamma+1)\left[\left[\frac{\Delta t}{t}\right]^2+\left[\frac{(1-\beta n)\Delta x}{x}\right]^2\right]^{1/2}, \quad (1)$$

with $t=x/\beta c$. Here $\gamma=1+T/M$ and M is the neutron mass, x is the neutron flight-path length, t is the neutron flight time, Δt is the intrinsic time dispersion of the system, n is the refractive index of the scintillator material, and Δx is the neutron path uncertainty arising from the finite thickness of the counter. The effective thickness of the counter is reduced from its physical thickness Δx by the factor $(1-\beta n)$. (The thickness of the counter contributes to the energy resolution ΔT only because there exists a difference between the neutron speed and the speed of light in the scintillator.)

The time dispersion Δt was obtained from the observed widths of the prompt gamma peaks in the TOF spectra. Measured time dispersions were about 0.8 ns for the NE-102 plastic scintillators and about 1.1 ns for the NE-213 liquid scintillators. The energy resolutions calculated from the above equation ranged from 0.25 MeV at 5 MeV neutron energy to about 5 MeV at 90 MeV neutron energy.

E. Conversion to energy spectra

The prompt gamma peak in each TOF spectrum provided a reference point for calculating absolute neutron flight times. The background-subtracted TOF spectra were converted to energy spectra with bin widths equal to integral multiples of the calculated experimental energy resolutions. To improve statistics, energy spectra from the NE-102 detectors were binned at twice the calculated ener-

gy resolutions; those from the NE-213 detectors were binned at three times the calculated energy resolutions for bins below 20 MeV and at twice the calculated energy resolutions for bins above 20 MeV neutron energy. No structure in the continua is observed in the energy spectra which would be affected by this binning. Absolute cross sections were obtained by dividing each energy spectrum by the number of projectiles incident on the target, the calculated neutron detector efficiency, and the detector solid angle.

F. Neutron detector efficiency calculations

The neutron detection efficiency of each counter was calculated with the Monte Carlo code of Cecil *et al.*[17] Calculations with this code provide good agreement with many experimental measurements of neutron detector efficiencies for neutron energies from about 1 to 300 MeV and for detector thresholds from about 0.1 to 22 MeV ee. The calculated efficiencies used for both types of scintillator counters are plotted in Fig. 5. For the NE-213 counters, the contribution from the (n,γ) channel was removed in the calculations since pulse-shape discrimination was used to eliminate gamma-ray events for those counters.

G. Corrections

Absolute cross sections were corrected for the dead-time losses in the data-acquisition system. The live time was measured directly as the ratio between the actual number of events recorded by the computer data-acquisition system and the number of (scaled) neutron events detected by the neutron counters. The resultant dead-time correction was typically 1% to 4%.

No correction was made for neutron losses in the n-γ discrimination analysis of the NE-213 counters because these losses were typically less than 0.2% as discussed in Sec. II. A correction was made for the ^{12}C(n,γ) reaction contributions to the NE-213 efficiencies. Since such interactions were eliminated by the n-γ discrimination, they were removed from the Monte Carlo calculation of the detector efficiencies. This correction was significant only in the neutron energy range from about 5 to 40 MeV, and resulted in a 1% to 2% correction to the NE-213 efficiencies.

The maximum neutron attenuation through the air was estimated to be less than 2% for the lowest neutron kinetic energy (5 MeV) observed in this experiment; no corrections were applied for this effect at neutron kinetic energies above 10 MeV where air transmission was nearly unity ($\geq$99.5%). Corrections were made for neutron attenuation ($\leq$3%) through the scattering chamber wall.

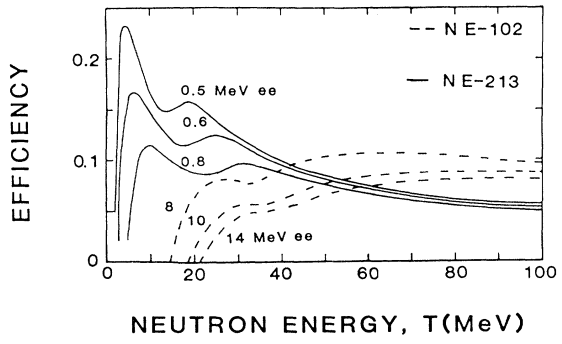

FIG. 5. Neutron detector efficiencies calculated with the Monte-Carlo code (Ref. 17) for a 5.08 cm diameter $\times$ 5.08 cm NE-213 liquid scintillator and a 12.7 cm diameter $\times$ 10.2 cm NE-102 plastic scintillator. The pulse-height thresholds are 0.5, 0.6, and 0.8 MeV ee for the NE-213 counter and 8.0, 10.0, and 14.0 MeV ee for the NE-102 counter.

H. Error analysis

The uncertainties associated with the final results are separated into relative and scale uncertainties. The relative uncertainties are primarily statistical and include contributions from the shadow-bar background subtractions. These relative uncertainties are typically a few percent and small compared to the overall scale uncertainties. The scale uncertainties, which arise from several separate contributing factors, are summarized in Table I. The beam integration was performed by collecting the beam in a reentrant Faraday cup approximately 12 m downstream of the target. An overall beam integration uncertainty of $<$5% was assumed based on earlier tests with similar Faraday cups at the Maryland Cyclotron Facility. Multiple scattering losses of the beam were calculated to be $\lesssim$1%. The target thicknesses were determined by measurement of the areas and weighing the foils. The net results were limited by the areal measurements and estimated to be accurate to better than 5%. The detector efficiency calculations for well-known thresholds were tested to be accurate to about 5% by comparison with several available neutron detector efficiency measurements.[17] The uncertainty in the pulse-height calibrations for the neutron detectors introduces another uncertainty into the efficiencies which are a function of the threshold applied. The overall detector efficiencies are estimated to be accurate to about $\pm$7—10%. Finally, the uncertainties in the solid angle, the live time correction, and the n-γ discrimination are all estimated to be small. The overall uncertainty is estimated to be $\pm$12%.

IV. EXPERIMENTAL RESULTS

The measured neutron-energy distributions for the four targets studied are presented and discussed briefly in Sec. IV A for the proton-beam measurements and in Sec. IV B for the alpha-beam measurements. More complete analyses of the spectra are provided in Secs. V and VI, where they are compared with emitted proton spectra and vari-

TABLE I. Scale uncertainties (%).

Beam integration	5
Target thickness	5
Detector efficiency	7—10
Neutron attenuation	2
Solid angle	$<$0.5
Live time	$<$1.0
n-γ losses	$<$1.0
Overall	12

ous model calculations, respectively. The experimental spectra are presented for laboratory angles from 20° to 135° and for neutron kinetic energies from about 5 MeV up to the maximum, kinematically allowed, neutron energies ($\lesssim$150 MeV). The energy and angular ranges in the spectra for the heavy targets, especially for the alpha-induced spectra, were limited by the available beam time. The spectra are plotted on the same scales to facilitate comparisons of their relative cross sections.

A. The (p,n) distributions

Figure 6 shows the measured neutron inclusive spectra for the proton-beam measurements. The spectra reveal three distinct energy regions: a low-energy, or evaporation region, a high-energy region dominated by the quasifree scattering process, and an intermediate region sometimes referred to as the preequilibrium region. The low-energy portions of the observed spectra are more nearly isotropic than the higher-energy regions and are characterized by an observed exponential falloff in the cross sections with increasing energy. Unfortunately, the neutron spectra do not extend to low enough energy in order to extract nuclear temperatures reliably. The high-energy portions at the forward angles also show a nearly exponential decrease in the cross section. The intermediate or preequilibrium region is seen to be relatively flat at the forward angles but smoothly changing to an exponential decrease with energy at wide angles. In Sec. V, we compare the measured neutron spectra with quasifree scattering, preequilibrium, intranuclear-cascade, and evaporation-model calculations.

B. The (α,n) distributions

The alpha-induced neutron spectra are shown in Fig. 7. Fewer measurements were performed than for the proton-beam experiment, particularly at backward scattering angles and for the low-energy portions of the neutron spectra. No high-energy (NE-102 detector) measurements were performed for the Bi target. Nevertheless, certain characteristic features can be identified in the neutron spectra. The low-energy portions display large cross sections which decrease exponentially with increasing energy characteristic of equilibrium or evaporation-type processes. The high-energy portions of the spectra are observed to extend up to neutron kinetic energies over 100 MeV. The exponential decrease of the high-energy portions of the neutron spectra are due to the Fermi-momentum distribution of the projectile neutrons plus nucleon-nucleon correlations in the target and projectile nuclei. In his analysis of inclusive proton data from ($\sim$0.7 GeV) protons on light-target nuclei ($A \lesssim 9$), Gurvitz[18] showed that high-momentum portions of the proton spectra could be described well with a universal one-nucleon momentum distribution function of the $(A-1)$ recoil nucleons.

The two complete (i.e., with both low- and high-energy measurements) 45° spectra (viz., for Al and Zr) show a distinct "shoulder" in the neutron spectrum near 35 MeV, the beam energy per nucleon. This shoulder may be attributed to neutron emission from single or only a few nucleon-nucleon scattering steps between the nucleons in the projectile with the nucleons in the target. That this energy region shows such a large deviation from the ex-

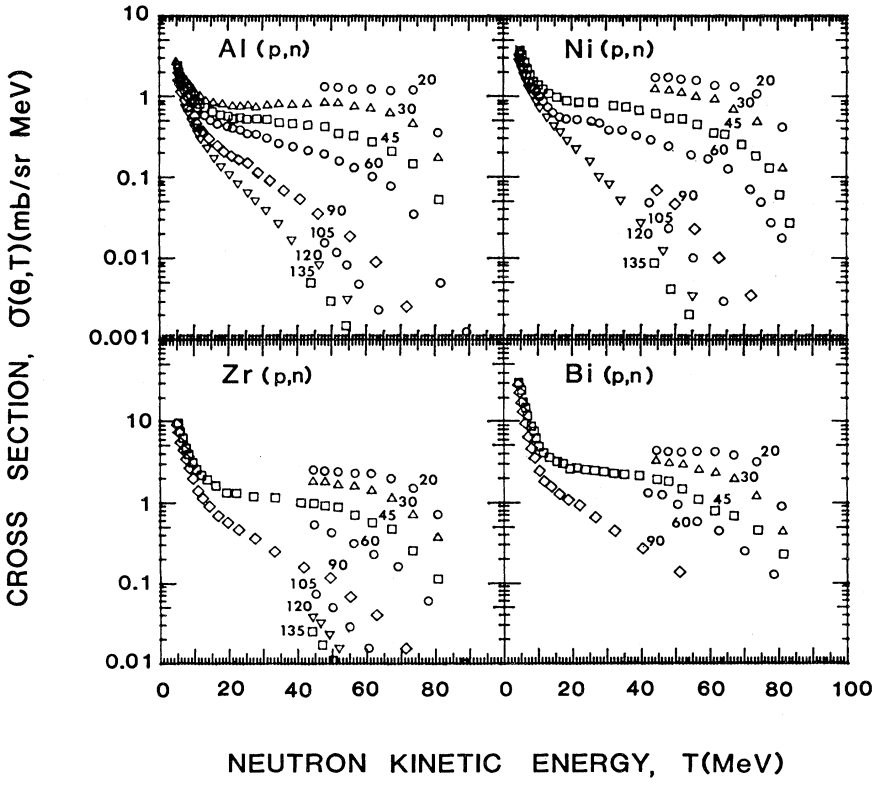

FIG. 6. The laboratory doubly differential cross sections of neutrons resulting from 90-MeV proton bombardment of ^{27}Al, ^{58}Ni, ^{90}Zr, and ^{209}Bi.

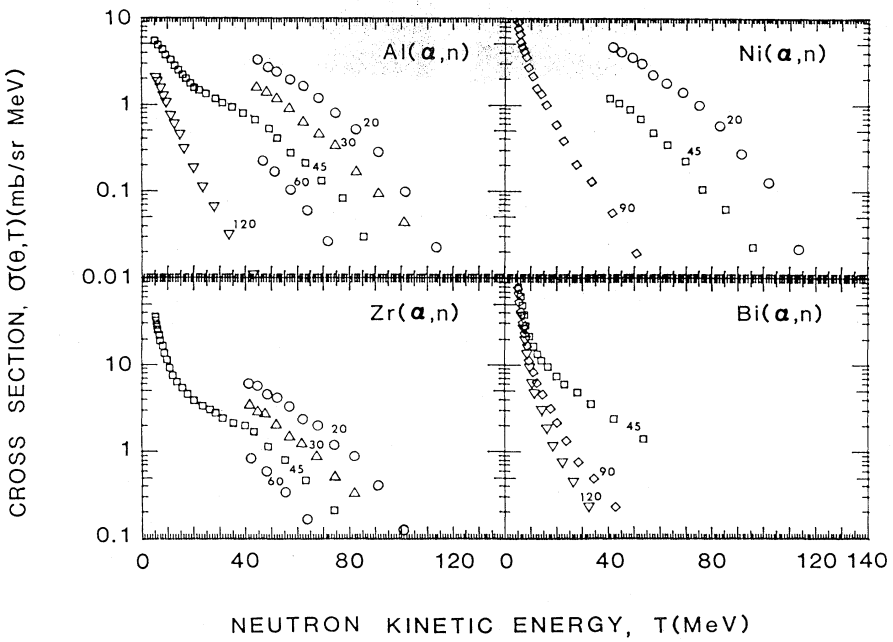

FIG. 7. The laboratory doubly differential cross sections of neutrons resulting from 140-MeV alpha-particle bombardment of ^{27}Al, ^{58}Ni, ^{90}Zr, and ^{209}Bi.

ponential energy dependences observed at lower and higher energies indicates that such nucleon-nucleon scattering processes are significant. Unfortunately, no complete measurements (i.e., of both the high- and low-energy portions of the spectra) were performed at more forward angles where the quasifree scattering process might reveal a distinct peak. The emitted proton measurements of Wu *et al.*[2] for 140 MeV alpha-particle bombardment of the same targets do reveal such a peak at more mechanisms in the different parts of the spectra.

V. COMPARISONS WITH EMITTED-PROTON SPECTRA

In order to facilitate direct comparisons of emitted neutron and proton spectra, the (p,n) and (α,n) measurements reported here were performed on the same target nuclei, and at the same incident beam energies and angles as the earlier (p,p') and (α,p) measurements of Wu *et al.*[2,3] In Sec. VI, we present comparisons of various theoretical calculations with the measured (p,n) spectra. In this section we first compare the measured emitted proton and neutron spectra in order to infer a qualitative but model-independent understanding of the dominating reaction

A. Comparison of the (p,n) and the (p,p') inclusive spectra

Typical (p,n) spectra at two angles are compared in Fig. 8 with the (p,p') spectra of Wu *et al.*[2] for ^{27}Al, ^{58}Ni, ^{90}Zr, and ^{209}Bi. Comparisons at other angles show the same features. In the low-energy ($\leq$25 MeV) region of the spectra, the neutron yields are comparable to the proton yields for low-A target spectra (viz., ^{27}Al), but become considerably larger for high-A target spectra (viz., ^{209}Bi). Furthermore, both the neutron and the proton yields are nearly isotropic in this low-energy region, especially for the higher-A targets. These characteristic features are consistent with the assumption that the low-energy nucleon yields are dominated by equilibrium processes such as evaporation from a residual compound nucleus. The suppression of the emitted proton spectra compared to the emitted neutron spectra at low energies for the large-A targets results simply from the large Coulomb barrier present for protons in a nucleus with a large-Z value.

In the high-energy ($>$30 MeV) region, the neutron and

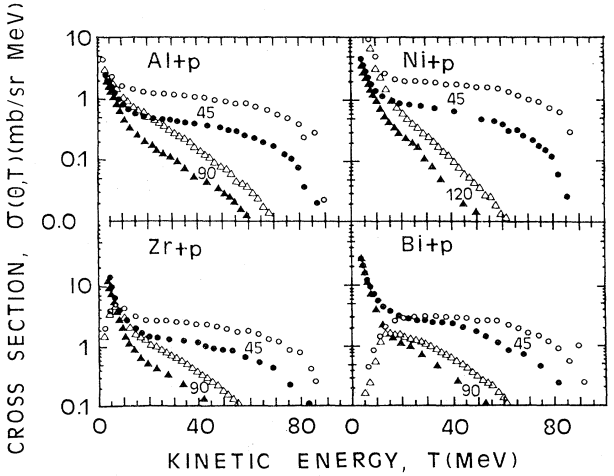

FIG. 8. A comparison of proton (open symbols) and neutron (closed symbols) cross sections at 45° and 90° or 120°, as indicated, from 90-MeV protons on ^{27}Al, ^{58}Ni, ^{90}Zr, and ^{209}Bi.

proton spectra are similar in shape for all the target nuclei. Beyond the evaporation region, the neutron yields are about one-half the proton yields. This ratio can be understood in terms of a simple counting argument and the dominance of the one-step "quasifree" scattering mechanism in the high-energy region. For single-step quasifree nucleon-nucleon scattering, an incident-proton interaction with a target proton can contribute only to the yield of protons, whereas an incident-proton interaction with a target neutron can contribute to both the proton and neutron yields. Thus, the ratio of protons to neutrons emitted from a target with N neutrons and Z protons is expected to be approximately

$$\frac{\sigma(\mathrm{p,p'})}{\sigma(\mathrm{p,n})}=\frac{Z\sigma_{\mathrm{pp}}+N\sigma_{\mathrm{pn}}}{N\sigma_{\mathrm{pn}}}\ , \tag{2}$$

where σ_{pp} and σ_{pn} are effective differential cross sections for p-p and p-n scattering,[19] respectively, which represent averages over the quasifree scattering angle and energy of the proton and the target nucleon. (Note that σ_{pp} is the experimentally measured differential cross section and therefore *includes* a factor of 2 for the fact that two protons are emitted in the final state.) Using the differential cross section at $\theta_{\mathrm{c.m.}}=90°$ (which corresponds to $\theta_{\mathrm{lab}}=45°$, where the proton and neutron spectra are compared) and an effective exit-channel energy of about 70 MeV, we find that this crude expression gives approximately the observed ratios for all four targets: the observed ratios decrease from about 2.5 for ^{27}Al to 1.7 for ^{209}Bi while Eq. (2) gives roughly 1.9 and 1.5, respectively. In contrast, the ratio for equilibrium-type processes would depend on, in addition to the neutron-to-proton ratio, the Q values as well as Coulomb and angular-momentum barriers, and would not be expected to exhibit any simple dependence on Z and N. In Sec. VI, we will show that the observed high-energy neutron-to-proton ratios are consistent also with the predictions of a quantitative quasifree scattering model calculation.

B. Comparisons of the (α,n) and the (α,p) inclusive spectra

The alpha-induced neutron spectra are compared with the proton spectra in Fig. 9 for the three target nuclei ^{27}Al, ^{90}Zr, and ^{209}Bi. Similar to the proton-beam results, we see that for the low-Z target (viz., ^{27}Al), the neutron and proton evaporation (i.e., low-energy) yields are comparable; whereas for the high-Z target (viz., ^{209}Bi), the proton-evaporation yield is considerably suppressed by the Coulomb barrier. There is a noticeable increase in net evaporation emission of nucleons from alpha-induced reactions compared to proton-induced reactions.

In the energy region near and above the incident beam energy per nucleon, the neutron and proton spectra show very similar spectral shapes including slopes which are essentially identical. As discussed in Sec. IV B, the "shouldering" of the alpha-induced continuum spectra at about the beam energy per nucleon (35 MeV) may be attributed to appreciable contributions to the continuum from simple or few nucleon-nucleon scattering processes between nucleons in the projectile and nucleons in the target nucleus. Such quasifree interactions with alpha-particle beams will produce approximately equal yields of protons and neutrons. The ratio of protons to neutrons emitted from a target nucleus of N neutrons and Z protons should be approximately

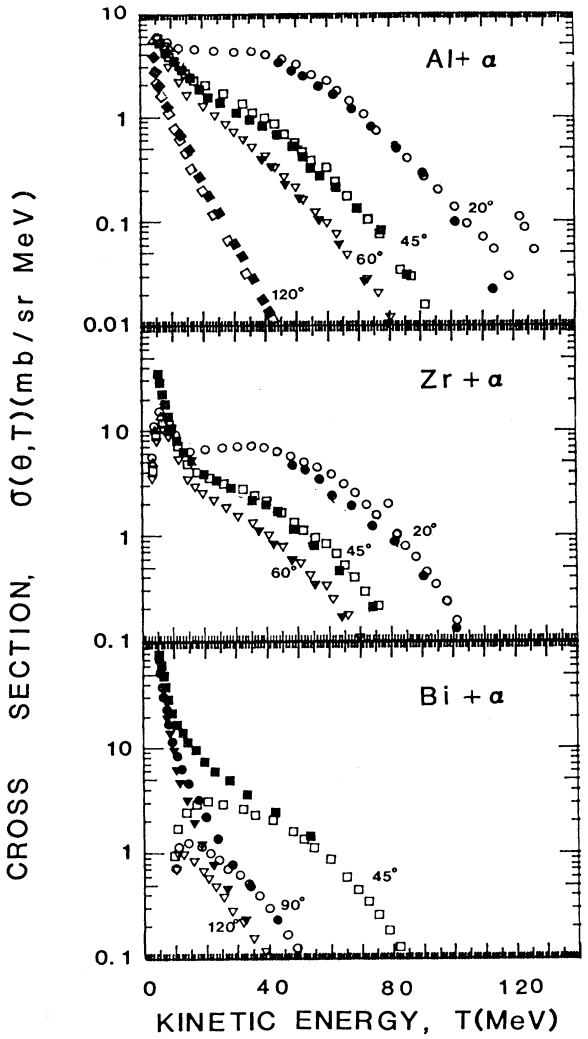

FIG. 9. A comparison of proton (open symbols) and neutron (closed symbols) cross sections from 140-MeV alpha-particle bombardment of ^{27}Al, ^{90}Zr, and ^{209}Bi.

$$\frac{\sigma(\alpha,x\mathrm{p})}{\sigma(\alpha,x\mathrm{n})}=\frac{2(Z\sigma_{\mathrm{pp}}+Z\sigma_{\mathrm{np}}+N\sigma_{\mathrm{pn}})}{2(N\sigma_{\mathrm{nn}}+Z\sigma_{\mathrm{np}}+N\sigma_{\mathrm{pn}})}\ . \tag{3}$$

For nucleon-nucleon effective cross sections taken at $\theta_{\mathrm{c.m.}}=90°$ and at an effective collision energy of about 20 MeV, the predicted values are in good agreement with the observed ratios (see Fig. 9) of about 1.0, 1.0, and 0.9, taken at the beam energy per nucleon in the forward angle ($\lesssim 45°$) spectra.

At forward angles, the alpha-beam measurements show a characteristic shoulder-arm type of spectrum[20,21] as described by Nagamiya *et al.*[20] for high-energy heavy-ion reactions. The spectra gradually change into a smooth exponential falloff at wider angles. The break in the shoulder-arm spectra is seen to occur near the incident

beam energy per nucleon (35 MeV). The arm part of the emitted proton and neutron spectra is an exponential fall-off which extends up to more than three times the beam energy per nucleon. Such energetic nucleons could not be emitted if the target and projectile nuclei were simply assemblies of protons and neutrons without any mutual interactions. Thus, this part of the spectra reflects nuclear effects such as Fermi motions of the projectile nucleons, short-range correlations between nucleons in both the target and projectile nuclei, and alpha-nucleon quasifree knockout. Note that this part of the spectrum is not observed in the proton-beam measurements where nucleon production above the beam energy (which equals beam energy per nucleon) is energetically impossible.

VI. COMPARISONS WITH THEORETICAL CALCULATIONS

Various theoretical models were developed to describe scattering mechanisms responsible for the large nuclear continuum observed at intermediate energies. Serber[12] pointed out the importance of single N-N scattering within a nucleus when the wavelength of the incident nucleon is short relative to internucleon distances. Bertini[22] used the intranuclear-cascade (INC) model to explore this quasifree scattering process by requiring all the collision positions to be within the nucleus, while energies and directions of colliding particles are followed explicitly in a three-dimensional geometric scattering model. The INC model was applied successfully at high bombarding energies.[23] Also, assuming single N-N scattering, the quasifree (QF) model accounted for much of the high-energy continuum at forward angles, assuming that single-step processes dominate this portion of the continuum.[1,8,11] Both the INC and the QF models predict poorly the low-energy continuum where high-temperature components from equilibrium processes dominate the continuum spectrum. In formulating the preequilibrium (PE) model to account for these effects, Griffin[24] proposed a semiclassical multistep reaction mechanism consisting of excited particle-hole stages, each with a probable emission of particles into the continuum as the excited compound nucleus proceeds toward equilibration. The PE model, as modified by Blann[25,26] to predict absolute yields, can be expected to fit broader ranges of the continuum. The model was limited to predictions of angle-integrated yields. The PE model was further modified by Blann[27] to include effects of particle-hole interactions in the diffuse nuclear surface using the geometry-dependent hybrid model. Theoretical attempts to formulate multistep models that predict angular distributions of particles emitted into the continuum include two limiting approaches to the statistical theory of multistep compound and direct reactions: quantum-mechanical formulations by Feshbach *et al.*[28] and by Tamura *et al.*[29] and, as in the PE model of Blann, a semiclassical formulation by Mantzouranis *et al.*[30] Several applications of these quantum-mechanical formulations were reported.[31,32] The PE model of Mantzouranis *et al.* was used[30,33] to predict angular distributions. We present comparisons of the measured continuum spectra with the predictions of the QF, the PE, and the INC models.

A. Comparisons with quasifree-scattering calculations

The importance of the nucleon-nucleon scattering mechanism in medium-energy nuclear reactions has been discussed for many years. Wall and Roos[1] noted broad peaks in their (p,p′) spectra at an incident energy of 160 MeV which show the signature of quasifree scattering from a bound target nucleon; i.e., the peaks move with the same kinematical relation as that for free nucleon-nucleon scattering. Cowley *et al.*[6] and Alexander *et al.*[34] concluded that at intermediate energies, nucleon-nucleon scattering appears to act as a doorway process leading to more complicated scattering mechanisms. Wu[11] showed that a simple plane-wave-impulse-approximation (PWIA) calculation can account for the high-energy portion of the proton continuum produced in (p,p′) reactions at 62 and 90 MeV.

In an earlier paper,[13] we presented comparisons of some of the neutron spectra reported here with the proton spectra of Wu *et al.*[2] Recall that the neutron measurements were performed at the same beam energy and with the same targets as the proton measurements in order to facilitate such comparisons. The earlier paper shows that the observed ratios between the emitted neutron and proton spectra are, in the high-energy portions of the forward-angle spectra, consistent with the ratios expected if the quasifree scattering process dominates the reactions. Furthermore, the earlier paper presents a comparison of PWIA quasifree scattering calculations for the emitted neutron and proton spectra from an aluminum target, which shows that both spectra can be fitted well simultaneously with the same normalization factors. In the earlier work, the quasifree calculations were performed only for the aluminum target because it was the lightest target studied and might be expected to show the clearest signature of quasifree scattering, and because the quasifree calculations require the specific binding energies of each subshell of the target nucleus and these binding energies are less well known for deep-lying shells of heavy nuclei. In this paper, we extend the comparisons of both neutron and proton spectra with the PWIA quasifree calculations to the nickel target also. The results for this intermediate-mass target are compared with those obtained earlier for aluminum. Unfortunately, the binding energies of low-lying shells in zirconium and bismuth are too uncertain to enable reliable calculations to be performed.

The quasifree calculations were performed in the PWIA and are of the form

$$\frac{d^2\sigma}{d\Omega\, dE} \propto \sum_i N_i \int_q \int_\phi \frac{q\, dq}{E_q} \mid \phi_i(\vec{q}) \mid^2 E_c^{\,2} \times \frac{d\sigma}{d\Omega}(E_c,\theta_c) d\phi \,, \tag{4}$$

where E_c and θ_c are the reaction energy and angle, respectively, in the center-of-mass system. This is the form used by Wu,[2] and Wall and Roos,[1] and is an extension of the form originally derived by Wolff.[35] The calculations use the free nucleon-nucleon scattering cross sections $d\sigma/d\Omega(E_c,\theta_c)$ which are taken to be the appropriate p-p and p-n cross sections obtained from experimental measurements. The integration is over the kinematic region of the struck nucleon Fermi momentum $\vec{q}$ such that the observed nucleon has the measured momentum. The quanti-

ty $\phi_i(\vec{q})$ is the Fourier tranform of the single-particle state wave function generated in a subroutine due to Chant[36] with binding energies and potential well geometries obtained from Elton and Swift.[37] The calculated proton and neutron spectra were normalized to the forward angle (30°) data by adjusting the number of nucleons N_i participating in the collision from each ith single-particle state. We stress that the calculations use the same normalizations for both the neutron and proton spectra. The outermost shell was weighted at 60% of the number of nucleons expected in the simple shell model, while the inner shells were each weighted at 20% of the numbers expected (since distortions may subsequently be large). Since these are plane-wave calculations, we know that *some* overall normalization is required.

In Figs. 10 and 11, we compare the (p,n) and (p,p') spectra with the results of the PWIA quasifree calculations for the aluminum and nickel targets, respectively. Although the calculated spectra underestimate the large-angle yields as expected, they agree to within ±15% with the high-energy portions of the forward-angle neutron and proton spectra. That these neutron and proton spectra are fitted simultaneously with the same normalization factors suggests that the single nucleon-nucleon scattering mechanism accounts for most of the continuum spectrum above the evaportation peaks at forward angles.

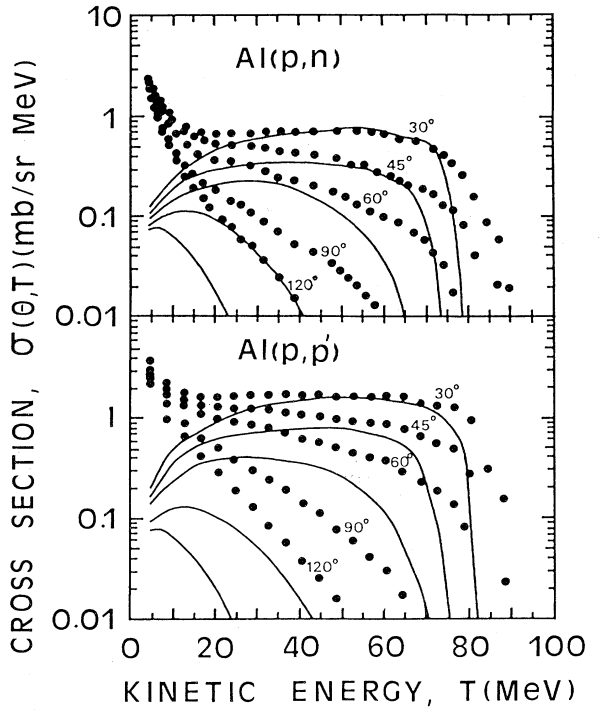

FIG. 10. Comparisons of neutron and proton cross sections from bombardment of ^{27}Al by 90-MeV protons with the predictions (solid lines) of a PWIA calculation for quasifree scattering (see text).

B. Comparisons with preequilibrium predictions

Even if we are able to convince ourselves that the nuclear reactions begin with quasifree interactions between individual nucleons, we know that the products of these initial interactions will have some probability for subsequent interactions before they can escape from a finite nucleus. One of the most promising models which attempts to describe the results of these later interactions is the so-called exciton preequilibrium model. This model represents the interaction of the projectile with the target in terms of the creation of particle-hole pairs, which are called excitons. The system is considered to be formed in a unique particle-hole configuration and to move toward statistical equilibrium through nucleon-nucleon scattering. The first collision term represents the direct-reaction term and higher-order terms represent multistep processes where all terms are formulated for reactions to the continuum. Particles are emitted from all the different kinds of states produced. The process can be described by a Boltzmann-type master equation for a Fermi-gas system.[38] Mantzouranis *et al.*[30,31] extended this model to provide both angular and energy distributions of absolute differential cross sections.

We present here comparisons with preequilibrium calculations based on the exciton and the geometry-dependent hybrid models. The first exciton model calculations are similar to those which were compared with emitted charge-particle spectra by Wu *et al.*[2] These calculations were performed with a code written by Wu and Chang[39] which was based on the formulation given by Cline and Blann.[40,41] The code uses a closed-form formalism and predicts only angle-integrated energy spectra. The second set of calculations were performed using the exciton model as developed by Mantzouranis *et al.*[30,31] and can predict angular distributions using a recursion relation as discussed by Machner.[33] The third set of preequilibrium calculations were based on the geometry-dependent hybrid model[27] with Blann's[42] improved nucleon-density functions and precompound parameters; these calculations include compound emissions.

In order to compare our experimental results with the predictions of the prequilibrium models, it was necessary to obtain angle-integrated neutron energy spectra. These spectra were obtained from the double-differential cross sections by integrating over laboratory angles. In order to obtain complete angle integrations, it was necessary to extrapolate the experimental spectra to angles more forward and backward than measured. The data were binned in 5 MeV intervals and plotted as angular distributions for each energy bin, as shown in Fig. 12. The integration was achieved by simple step summations over angular bins equal to the experimental laboratory-angle spacings. Figure 13 shows the resulting angle-integrated neutron spectra.

The corresponding experimental proton spectra reported by Wu *et al.*[2] are shown also in Fig. 13, and both sets of experimental results are compared with the exciton model calculations obtained with the code of Wu and Chang.[39] The predicted neutron and proton spectra are represented by the solid and dashed lines, respectively. The calculations assume level densities that are excitation-energy dependent and corrected for the pairing effect. The assumed particle-hole densities included Pauli exclusion as derived by Williams.[43] The equilibrium of the composite nucleus was allowed to proceed from the simplest "doorway" state (2p-1h) to a series of more complex "hallway"

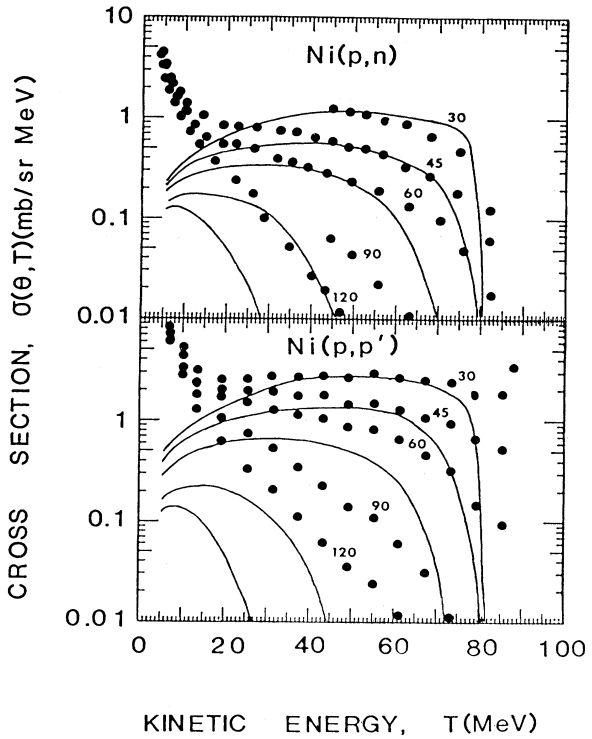

FIG. 11. Comparisons of neutron and proton cross sections from bombardment of ^{58}Ni by 90-MeV protons with the predictions (solid lines) of a PWIA calculation for quasifree scattering (see text).

states until the most probable exciton number was reached. The average two-body transition matrix elements were set empirically by Kalbach-Cline.[44] The calculations are absolute in magnitude and do not include complex-particle emission. As may be seen from Fig. 13, the predicted spectra generally reproduce the experimental nucleon spectra reasonably well for shape and approximately agree with the observed proton-to-neutron ratios; however, the calculations signficantly underestimate the high-energy continuum yields of both the emitted protons and neutrons. Figure 14 shows the combined precompound and compound-nucleus spectra calculated by Blann[42] with the geometry-dependent hybrid (GDH) model. In the calculation, the Fermi density function is parametrized using results of the Myers droplet model,[45] with an *ad hoc* range parameter assumed equal to the entrance-channel de Broglie wavelength. The intial exciton numbers resulting from different N-N interaction pairs are selected based on the relative strengths of the free N-N scattering cross sections σ_{np} and σ_{pp} weighted according to the Z and N values of the target nucleus. The GDH results reproduce the measured neutron and proton spectra remarkably well for shape and magnitude. The compound predictions agree with the evaporation-region spectra somewhat better for the heavy target spectra. The GDH-model calculations somewhat underestimate the continuum of the emitted proton and neutron spectra for the bismuth target.

In Fig. 15 we present the exciton-model calculations performed with the code of Machner for the angle-integrated spectrum. The predictions of Wu *et al.* are shown also for comparison. The results of Machner are seen to be very similar in shape to those of Wu *et al.*, but

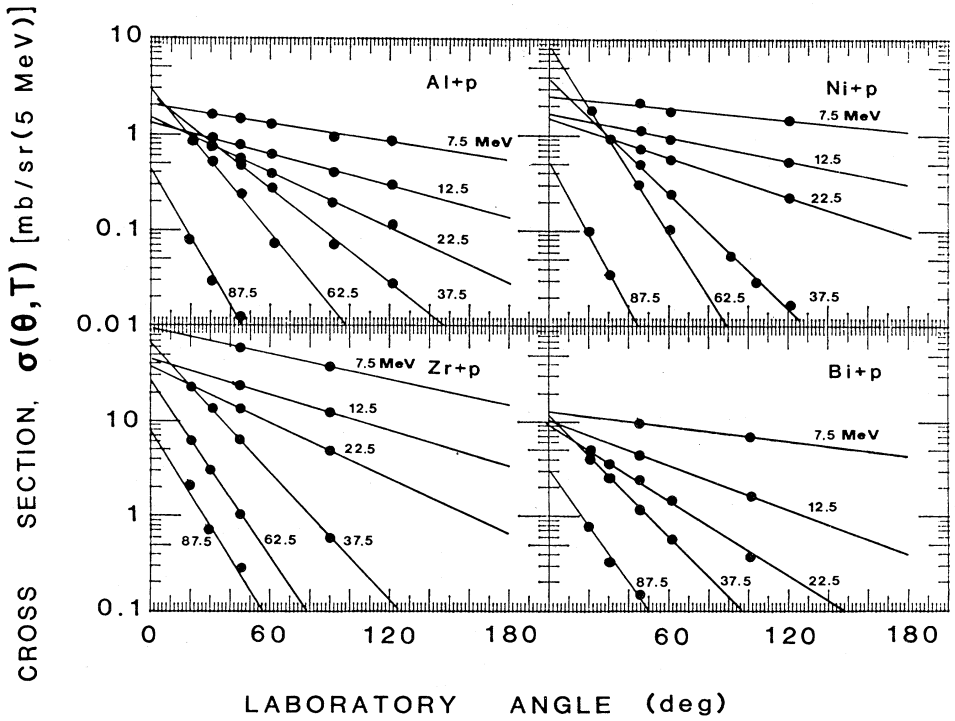

FIG. 12. The angular distributions of 5-MeV energy bins at neutron kinetic energies of 7.5, 12.5, 22.5, 37.5, 62.5, and 87.5 MeV in the laboratory frame.

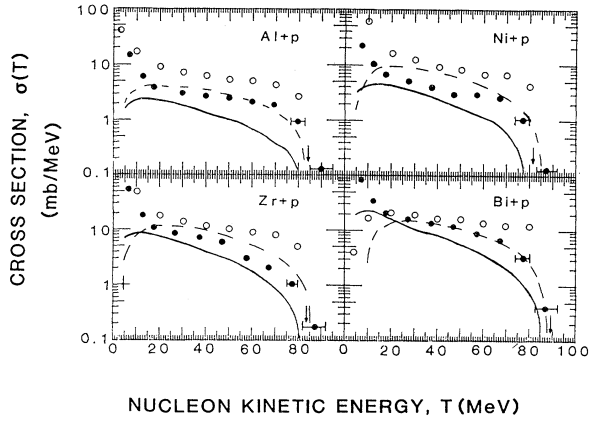

FIG. 13. Laboratory-angle-integrated cross sections of neutrons (closed circles) and protons (open circles) from 90-MeV protons on ^{27}Al, ^{58}Ni, ^{90}Zr, and ^{209}Bi. The arrows indicate the kinematic maximum neutron energy for these targets. The horizontal error bars represent the energy resolution for the high-energy measurements. The solid and dashed lines are preequilibrium exciton model predictions for neutrons and protons, respectively (Ref. 39 and this work).

in better absolute agreement with the experimental results. Based on the approach given by Mantzouranis *et al.*,[31] the angular decay rate is taken as the usual angle-independent exciton-model decay rate modified by an angular distribution function recursive on the number of excited particles and holes. The differential cross section is then taken as a sum over contributions from all exciton stage decay rates, each weighted by its average exciton lifetime. (More details on the calculations may be found in Ref. 33 and references therein.) Thus, this model provides predictions for angular dependence and these predictions for the aluminum target are compared with the experimental results in Fig. 16. At forward angles, the predicted differential cross sections overestimate the low-energy continuum data and underestimate the high-energy continuum. At large angles, the predicted and measured neutron yields are in rather good agreement everywhere. Since these calculations are absolute in magnitude, they clearly provide a good starting point for future improved calculations of angular dependence in the preequilibrium exciton model.

C. Comparison with intranuclear cascade calculations

The INC predictions reported here are calculations performed by Bertini[46] for 100 MeV protons incident on ^{27}Al and ^{208}Pb. Considered in these early INC calculations were the Fermi motions of the bound nucleons and their binding energies, the diffuseness of the nuclear surface, and potentials as functions of the nuclear radius. Although the Pauli principle was included in the calculations, they excluded boundary effects such as reflection and refraction, which were later shown[47] to have a bearing on the spectrum of secondary particles. The calculated spectra represent averages over large angular intervals; thus, the 45°, 90°, and 150° spectra are averaged over the angular regions 30° to 60°, 60° to 120°, and 120° to 180°, respectively. To obtain the neutron and proton differential cross sections appropriate to the 90 MeV proton bombarding energy of this experiment, we scaled down the emitted nucleon energy by a factor of 0.9 and reduced the differential cross sections at 100 MeV by the ratio of the total inelastic cross sections at 90 MeV to those at 100 MeV. The value for the total inelastic cross section at 90 MeV was obtained by interpolating linearly between the calculated INC values at 50 and 100 MeV.

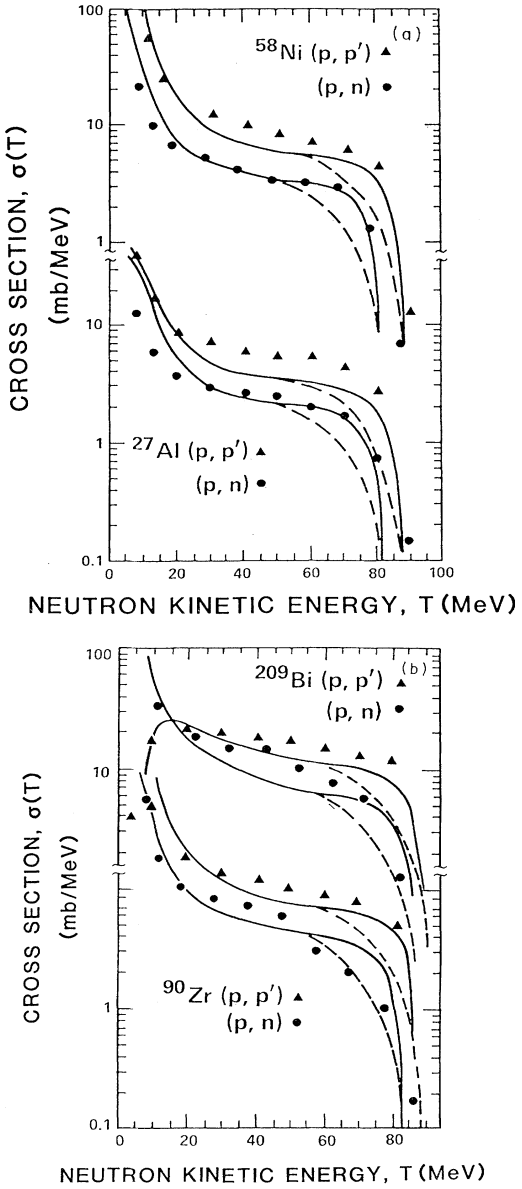

FIG. 14. Laboratory-angle-integrated cross sections of neutrons (circles) and protons (triangles) from 90-MeV protons on ^{27}Al, ^{58}Ni, ^{90}Zr, and ^{209}Bi. The solid lines are preequilibrium, geometry-dependent hybrid-model predictions (Ref. 42). The dashed lines are hybrid calculations.

Figure 17 illustrates the INC results compared with the measured neutron and proton spectra for ^{27}Al and ^{209}Bi nuclei. For the emitted neutron spectra, the calculations overestimate severely the forward-angle data of the light-target spectra; the calculated 90° spectrum agrees in shape

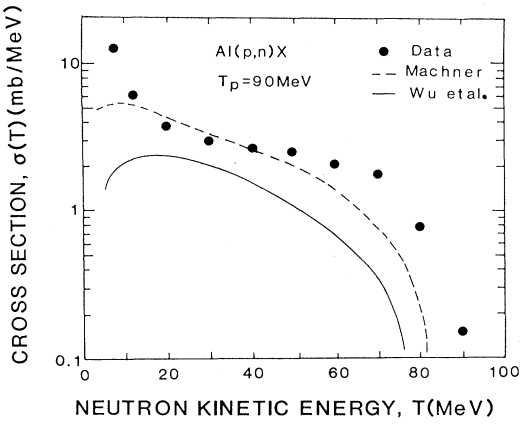

FIG. 15. Comparison of the angle-integrated cross sections from the ^{27}Al(p,n)X reaction with the exciton-model predictions calculated by Machner (Ref. 33 and this work). The predictions of the exciton model of Wu *et al.* (Ref. 39) are shown also for comparison.

but not in magnitude with the data; however, the predicted spectra for ^{208}Pb reproduce remarkably well the measured spectra for ^{209}Bi. The apparent discrepancies at the very-low energy end of the continuum are expected since the calculations do not include evaporation. For the emitted proton spectra, the INC reproduces only the forward-angle spectrum of the light target and the backward-angle spectrum of the heavy target. The INC model calculations seem to predict a proton-to-neutron ratio much smaller than either experimentally observed or theoretically obtained with previous models.

VII. CONCLUSIONS

Both the proton-induced and alpha-particle—induced neutron continuum spectra reveal signatures corresponding to both direct or single-step processes and multistep processes. At very low energies ($\lesssim$10MeV), evaporation yields are seen which are characteristic of equilibrium processes as well.

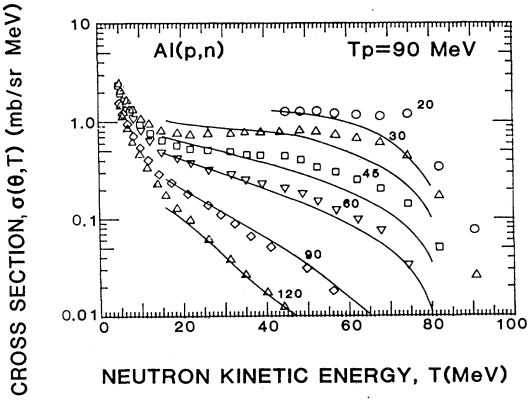

FIG. 16. Comparison of the doubly differential cross sections for the ^{27}Al(p,n)X reaction with the exciton-model predictions as calculated by Machner (Ref. 33 and this work).

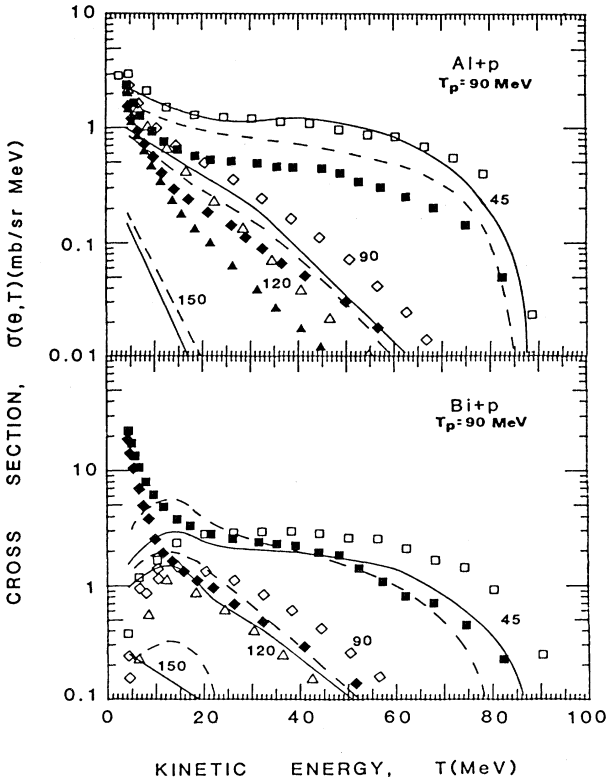

FIG. 17. Comparison of the measured neutron (closed symbols) and proton (open symbols) doubly differential cross sections with intranuclear cascade model predictions (Ref. 46) at 45°, 90°, and 150° spectra for the reactions ^{27}Al(p,n)X and ^{208}Pb(p,n)X [assumed the same as ^{209}Bi(p,n)X]. (The calculated spectra, originally obtained at 100-MeV incident-proton energy, were reduced to 90-MeV proton-induced spectra as described in the text.)

The proton-induced neutron spectra reveal shapes similar to those observed in emitted proton spectra, except at low energies for heavy targets where Coulomb barriers suppress the proton evaporation peaks, but have no effect on the neutron spectra. The most striking difference between the emitted neutron and proton spectra for the three lightest targets is that the magnitudes of the proton spectra are 2 to 3 times larger than the magnitudes of the neutron spectra (except in the evaporation regions). This difference is understood simply in terms of the dominance of the single nucleon-nucleon scattering process, at least as a doorway mechanism, and in terms of a simple counting argument for an incident proton striking a target nucleus with Z protons and N neutrons. Consistent with this picture, the magnitudes of the emitted neutron and proton spectra from incident alpha-particle bombardment are more nearly equal (except in the evaporation regions).

For the proton-induced measurements, the high-energy portions of the forward angle spectra are fitted well by a simple quasifree scattering calculation. These calculations include reasonable, but arbitrary, normalization factors; however, it is signficant that both emitted neutron and proton spectra are fitted simultaneously using the *same* normalization factors. The lower-energy and wide-angle spectra are severely underestimated by the quasifree

scattering calculations, indicating that additional strength in multistep processes is significant in these regions. Comparisons with preequilibrium exciton-model calculations show improved agreement in these regions; comparisons with preequilibrium, geometry-dependent hybrid model predictions show even better agreement. The exciton-model calculations are absolute in magnitude and consistently underestimate the measured neutron and proton spectra; the hybrid-model reproduces the shapes and magnitudes of both the light- and heavy-target spectra rather well. The calculations of Machner, which predict angular distributions, generally underestimate the high-energy portions of the forward-angle spectra, but predict the backward-angle spectra reasonably well; these calculations are encouraging, since they provide approximate agreement with no arbitrary normalizations.

The forward-angle neutron spectra from the alpha-particle bombardment of the various nuclei show a characteristic shoulder-arm type of spectrum. The shouldering is observed at approximately the beam energy per nucleon (viz., 35 MeV) at the most forward angles and moves downward in energy with increasing angle consistent with the kinematics of quasifree scattering between nucleons. The neutron spectra above the shoulder reveal an exponential dropoff presumably reflecting the Fermi motions and correlations in the target and projectile nucleons. This region is kinematically forbidden for incident protons.

In summary, these neutron spectra provide important comparisons with similar proton spectra and model calculations and further support the idea that medium-energy nuclear reactions proceed through the quasifree nucleon-nucleon scattering mechanism as a doorway state.

ACKNOWLEDGMENTS

The authors are grateful to Dr. Marshall Blann for communicating results of his calculations prior to publication. This work was supported in part by the National Science Foundation.

---

*Present address: National Cancer Institutes, Bethesda, MD 20205.

†Present address: Lawrence Berkeley Laboratory, Berkeley, CA 94720.

‡Present address: Bell Laboratories, Naperville, IL 60540.

[1]N. S. Wall and P. G. Roos, Phys. Rev. 150, 811 (1966); and T. Chen, R. E. Segel, P. T. Debevec, J. Wiggins, P. P. Singh, and J. V. Maher, Phys. Lett. 103B, 192 (1981).

[2]J. R. Wu, C. C. Chang, and H. D. Holmgren, Phys. Rev. C 19, 698 (1979).

[3]J. R. Wu, C. C. Chang, and H. D. Holmgren, Phys. Rev. C 19, 659 (1979).

[4]J. R. Wu, C. C. Chang, and H. D. Holmgren, Phys. Rev. C 19, 370 (1979).

[5]F. E. Bertrand and R. W. Peelle, Phys. Rev. C 8, 1045 (1973); Oak Ridge National Laboratory Report ORNL-4455, 1967; Oak Ridge National Laboratory Report ORNL-4450, 1969; Oak Ridge National Laboratory Report ORNL-4460, 1969; Oak Ridge National Laboratory Report ORNL-4469, 1970; Oak Ridge National Laboratory Report ORNL-4471, 1970; Oak Ridge National Laboratory Report ORNL-4638, 1971; H. W. Bertini, T. A. Gabriel, and R. T. Santoro, Oak Ridge National Laboratory Report ORNL-4311, 1972; J. W. Wachter, Oak Ridge National Laboratory Report ORNL-4903, 1973.

[6]A. A. Cowley, C. C. Chang, H. D. Holmgren, J. D. Silk, D. L. Hendrie, R. W. Koontz, P. G. Roos, C. Samato, and J. R. Wu, Phys. Rev. Lett. 45, 1930 (1980).

[7]J. W. Wachter, R. T. Santoro, T. A. Love, and W. Zobel, Bull. Am. Phys. Soc. 18, 118 (1973); 18, 1601 (1973).

[8]A. Galonsky, R. R. Doering, D. M. Patterson, and H. W. Bertini, Phys. Rev. C 14, 748 (1976).

[9]F. C. Maienschein, T. V. Blosser, H. R. Brashem, Oak Ridge National Laboratory Report TID-7652, 1963, p. 523.

[10]H. D. Holmgren, Bull. Am. Phys. Soc. 25, 600 (1980).

[11]J. R. Wu, Phys. Lett. 44, 1579 (1980).

[12]R. Serber, Phys. Rev. 72, 1008 (1947).

[13]B. D. Anderson, A. R. Baldwin, A. M. Kalenda, R. Madey, J. W. Watson, C. C. Chang, H. D. Holmgren, R. W. Koontz, and J. R. Wu, Phys. Rev. Lett. 26, 226 (1981).

[14]H. Knox and T. Miller, Nucl. Instrum. Methods 101, 519 (1972).

[15]P. Sperr, H. Spieler, and M. R. Maier, Nucl. Instrum. Methods 116, 55 (1974).

[16]R. A. Winyard, J. E. Lutkin, and G. W. McBeth, Nucl. Instrum. Methods 95, 141 (1971).

[17]R. A. Cecil, B. D. Anderson, and R. Madey, Nucl. Instrum. Methods 161, 439 (1979).

[18]S. Gurvitz, Phys. Rev. Lett. 47, 560 (1981).

[19]K. Chen, Z. Fraenkel, G. Frieldlander, J. R. Grover, J. M. Miller, and Y. Shimamoto, Phys. Rev. 166, 949 (1968).

[20]S. Nagamiya, M.-C. Lemaire, E. Moeller, S. Schnetzer, G. Shapiro, H. Steiner, and I. Tanihata, Phys. Rev. C 24, 971 (1981).

[21]R. A. Cecil, B. D. Anderson, A. R. Baldwin, R. Madey, A. Galonsky, P. Miller, L. Young, and F. W. Waterman, Phys. Rev. C 21, 2471 (1980).

[22]H. W. Bertini, Phys. Rev. 131, 1801 (1963).

[23]J. W. Wachter, W. A. Gibson, and W. R. Burrus, Phys. Rev. C 6, 1496 (1972).

[24]J. J. Griffin, Phys. Rev. Lett. 17, 478 (1966).

[25]M. Blann, Phys. Rev. Lett. 27, 337 (1971); 21, 1357 (1968).

[26]M. Blann, Annu. Rev. Nucl. Sci. 25, 123 (1975).

[27]M. Blann, Phys. Rev. Lett. 28, 757 (1972).

[28]H. Feshbach, A. Kerman, and S. Koonin, Ann. Phys. (N.Y.) 125, 429 (1980).

[29]T. Tamura, T. Udagawa, and H. Lemske, Phys. Rev. C 26, 379 (1982), and references therein.

[30]G. Mantzouranis, H. A. Weidenmuller, and O. Agassi, Z. Phys. A 276, 145 (1976).

[31]G. Mantzouranis, Phys. Lett. 83B, 25 (1976).

[32]R. Bonetti, L. Colli Milazzo, M. Melanotte, A. De Rosa, G. Inglima, E. Perillo, M. Sandoli, V. Russo, N. Saunier, and F. Shahin, Phys. Rev. C 25, 717 (1982).

[33]H. Machner, Phys. Lett. 86B, 129 (1979).

[34]Y. Alexander, J. W. Van Orden, E. F. Redish, and S. J. Wallace, Phys. Rev. Lett. 44, 1579 (1980).

[35]Peter Wolff, Phys. Rev. 87, 434 (1952).

[36]N. S. Chant, private communication.

[37]L. R. B. Elton and A. Swift, Nucl. Phys. A94, 52 (1967).

[38]G. D. Harp and J. M. Miller, Phys. Rev. C 3, 1847 (1971).
[39]J. R. Wu and C. C. Chang, Phys. Rev. C 16, 1812 (1977).
[40]C. K. Cline and M. Blann, Nucl. Phys. A172, 225 (1971).
[41]C. Kalbach-Cline, Nucl. Phys. A210, 590 (1973).
[42]M. Blann and H. K. Vonach, Lawerence Livermore Laboratory Report UCRL-88540, 1982; M. Blann, private communication.
[43]F. C. Williams, Jr., Nucl. Phys. A166, 31 (1971).
[44]C. Kalbach-Cline, Nucl. Phys. A172, 225 (1971).
[45]W. D. Myers, *Droplet Model of Atomic Nuclei* (Plenum, New York, 1977).
[46]H. W. Bertini, Phys. Rev. 162, 976 (1967).
[47]K. Chen, G. Friendlander, and J. M. Miller, Phys. Rev. 176, 1208 (1968).